Terahertz Sub-Wavelength Focusing and Negative Refraction Assisted Beam Transferring Based on 3-D Metamaterial Flat Lens Configurations

**Muthusamy Marishwari[1], Venkatachalam Subramanian[2],
Zhengbiao Ouyang[3], and Natesan Yogesh[4, *]**

Abstract—A flat lens made of a negative index (NI) metamaterial (MTM) focuses the diverging light waves with sub-wavelength resolution. However, to achieve tight 3-D focusing, one needs to realize a 3-D MTM with azimuthal and elevation focusing. In this work, a polarization-insensitive, wide-incident angle 3-D MTM showing an NI band of $0.34\,\text{THz}$ (37%) centered at $0.92\,\text{THz}$ is realized. A flat lens designed out of the proposed 3-D NI MTM shows sub-wavelength spot sizes of $0.48\lambda_1$ and $0.39\lambda_2$ for cylindrical electromagnetic (EM) waves emanating out of an electric dipole source, at $0.9\,\text{THz}$ and $0.95\,\text{THz}$, respectively. Also, the sub-wavelength focusing features of the NI flat slab are verified along non-symmetric planes by tilting the dipole source for different angles. It is also found that the finite flat slab configurations efficiently transfer EM beams for long conveyance lengths at NI frequencies. Thus, the realized flat slab configurations are useful for 3-D focusing requirements in optical trapping and imaging, and they are also useful for reducing the transmission losses associated with beam divergences.

1. INTRODUCTION

Negative-index (NI) metamaterials [1–3] are artificial materials that refract the incoming light rays on the same side of the optical normal as opposed to the conventional positive index materials. Emerging NI MTM lenses [4, 5] have generated great attention in the field of optical spectroscopy and imaging devices, and in the THz regime [6, 7], due to their high-resolution imaging characteristics by overcoming the optical diffraction limit. Studies based on fundamental mechanisms of NI MTM structures enable rapid progress in device development that offers advanced control on light propagation and manipulation techniques [8–10]. Flat lenses with negative refractive index carry near-field information due to the restoration of the evanescent field [1, 2] leading to sub-wavelength resolution and high resolving features.

The functionality of focusing lenses made of artificially engineered structures such as NI-based MTMs and metasurfaces is influenced by polarization sensitiveness [11–13], decreased efficiency for non-normal incidences [14, 15], and 1-D or 2-D anisotropic functionalities [16–18]. These constraints adversely affect the resolution of the flat lens system, even if it is made of NI MTM. Hence, the fundamental building block of the flat slab (i.e., a unit cell) is supposed to have functionalities independent of the polarization of incoming waves, angle of incidence, and reduced anisotropic effects.

Realizing an isotropic MTM with several captivating functionalities remains a challenge. However, various interesting findings have been proposed and demonstrated recently, for achieving polarization

insensitivity with unit cells made of symmetrically oriented orthogonal components [19, 20]. A few studies on spherically symmetric unit cells [21–23] establish the functionalities independent of polarization and incident angles. We notice that all-angle negative refraction is realized using Weyl MTMs [24, 25] and dielectric MTMs [26, 27] along with reduced anisotropic effects.

In this work, we demonstrate a 3-D NI MTM under multiple polarizations and incident angles for the purpose of realizing a flat lens at THz frequencies. The proposed structure is spherically symmetric along all the principal directions with an NI bandwidth of 0.34 THz (37%) centered at 0.92 THz. The sub-wavelength focusing features of the proposed flat lens along azimuthal and elevation directions confirm 3-D focusing with a resolution higher than that of a conventional lens. The linearity and reciprocity of the position of the focal spot with the source establish the broad spatial working regions of the proposed lens.

The second intriguing feature of the NI MTM-based flat lens is that it can be efficiently employed as a beam translator [28]. Efficient beam transfer is highly warranted in the THz regime because the THz beam in air rapidly decays due to moisture content (For instance, a 1 W THz beam at 1 THz is attenuated to be 10^{-30} W after traveling 1 km [29]). Moreover, guiding the THz wave remains a challenge owing to the high loss from the finite conductivity of metals. For example, conventional metallic waveguides, which are mostly used for microwave guiding, cannot be preferred for THz waves. Also, due to the high absorption coefficient of dielectric materials, optical fibers used for visible and near-infrared radiation cannot support THz waves over a long distance.

An NI slab can fairly translate an EM beam [30, 31] with a high degree of spatial coherence for a normal incident finite aperture source. The requirement of translating electromagnetic energy emanating from a THz source can be met by stacking NI slabs for longer extents. Moreover, for the realization of integrated optic circuits, a medium that can precisely control the profile of the beam and the propagation without divergence is needed. Here, we numerically analyze the propagation of THz Gaussian beams in the proposed NI MTM medium for different layers of flat slabs. The comparison of electromagnetic wave translation in free space with that of the NI flat slab reveals the prospect of the proposed structure as an effective THz beam translator.

2. 3-D NI MTM AND ITS NEGATIVE REFRACTIVE INDEX CHARACTERISTICS

2.1. Unit Cell Design

The geometry of the unit cell of the proposed 3-D MTM is shown in Figs. 1(a) and (b). This armillary-sphere-like structure is composed of three cylindrical rings whose axes are oriented in mutually perpendicular directions with a common center. The rings are made of gold (electrical conductivity $\sigma = 4.561 \times 10^7 \, \text{Sm}^{-1}$) which is embedded in a dielectric cube with relative permittivity $\varepsilon_r = 2.67$. Practically, material such as Benzocyclobutene (BCB) serves as a suitable dielectric background material for THz frequencies with this dielectric permittivity. The inner radius of each cylindrical ring is
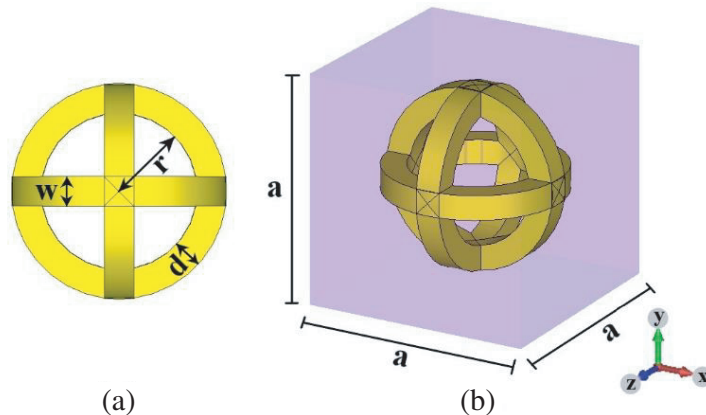

Figure 1. The unit cell of proposed 3-D NIM. (a) Cross-sectional view. (b) 3-D view.

$r = 40\,\mu\mathrm{m}$; the width of the circular cross-section is $w = 15\,\mu\mathrm{m}$; the depth of the cylinder is $d = 15\,\mu\mathrm{m}$; the lattice constant of the single unit cell is $a = 140\,\mu\mathrm{m}$.

2.2. Effective Material Parameters of 3-D NI MTM

The left-handed behavior of the designed NIM is analyzed from the transmission/reflection coefficients of the MTM numerically using the finite-integration-based EM solver CST Studio Suite. Fictitious waveguide boundaries [32] are applied to the unit cell which excites transverse electric (TE) and transverse magnetic (TM) plane waves. It should be noted that the fictitious waveguide setup used for the parameter retrieval resembles free space measurements, because its walls are made of perfect electric conductors (PEC), i.e., $\hat{n} \times \vec{E} = \vec{0}$, and perfect magnetic conductors (PMC), i.e., $\hat{n} \times \vec{H} = \vec{0}$, boundary conditions (BCs), such that it can support transverse electromagnetic (TEM) plane waves with $E_z = B_z = 0$, and therefore, it has no cut-off frequency. For a normal incident TE (TM) plane wave propagating along the z-axis, the two surfaces of the unit cell parallel to the yoz (xoz) plane, and those parallel to the xoz (yoz) plane are employed with PMC and PEC BCs, respectively. When the lattice constant is smaller than the wavelength of the light, this unit cell boundary setup is sufficient to get the transmission/reflection coefficients of the infinitely periodically arranged MTMs, as the MTM is effectively homogeneous. The propagation direction of the incident wave is along the z-axis, and the two surfaces of the unit cell parallel to the xoy plane are employed as the input/output excitation ports along with perfectly matched layer (PML) absorbing boundary conditions.

From the complex transmission (S_{21}) and reflection (S_{11}) coefficients, the effective parameters of the medium can be obtained using the standard retrieval procedure [32]. The relative wave impedance (z_r) and refractive index (n) in terms of scattering parameters are given by Equations (1)–(4) as follows:

$$z_r = \sqrt{\frac{\mu_r}{\varepsilon_r}} = \frac{1 + \Gamma_{12}}{1 - \Gamma_{12}} \tag{1}$$

$$n = \sqrt{\varepsilon_r \mu_r} = j\frac{c}{2\pi\nu t}\left[\ln|\tau| + j\arg(\tau)\right] \tag{2}$$

where t is the thickness of the medium, ν is the corresponding frequency, c is the velocity of light in free space, and

$$\tau = \frac{(S_{11} + S_{21}) - \Gamma_{12}}{1 - (S_{11} + S_{21})\,\Gamma_{12}} \tag{3}$$

$$\Gamma_{12} = \frac{1 - \left(S_{21}^2 - S_{11}^2\right)}{2S_{11}} \pm \sqrt{\left[\frac{1 - \left(S_{21}^2 - S_{11}^2\right)}{S_{11}}\right]^2 - 1} \tag{4}$$

By combining Equations (1) and (2), the effective material parameters such as relative dielectric permittivity ($\varepsilon_r' - j\varepsilon_r''$), relative magnetic permeability ($\mu_r' - j\mu_r''$), and refractive index ($n_r' - jn_r''$) are obtained. The usefulness of negative refraction can be established by calculating the figure of merit (FoM) as $|n_r'/n_r''|$. The extracted effective material parameters are shown in Fig. 2.

The real parts of ε_r and μ_r are simultaneously negative in a region between 0.75 THz and 1.09 THz. Thus, the bandwidth of the negative refractive index region is 0.34 THz (37%). From Figs. 2(b) and 2(c), one can observe that the imaginary parts of ε_r and μ_r that represent the dielectric and magnetic losses are low for the proposed MTM design. For example, the ε_r and μ_r values are $\varepsilon_r = -0.53 - j0.0018$ and $\mu_r = -0.74 - j0.0038$ at 0.9 THz, and $\varepsilon_r = -0.42 - j0.0037$ and $\mu_r = -0.53 - j0.0014$ at 0.95 THz, respectively. It is observed that due to the high symmetricity of the structure, the NI region is the same in all incident directions under normal incidence.

The FoM obtained from the real and imaginary parts of the refractive index is quite high which indicates that the proposed NIM shows low transmission loss in the NI regime. It is also important to note that the extracted parameters of the MTM are similar when the Drude model for gold is used, as the operating frequency range is within 1.2 THz. The Drude parameters of gold are taken as plasma frequency, $\omega_p = 1.37 \times 10^{16}\,\mathrm{rad/s}$, damping frequency, $\gamma_p = 4.05 \times 10^{13}\,\mathrm{rad/s}$, and $\varepsilon_\infty = 1$.

Since the used retrieval procedure is not meant for finite slabs as it leads to branching problems, to verify the correctness of the retrieved parameters, the homogenization error percentage is calculated
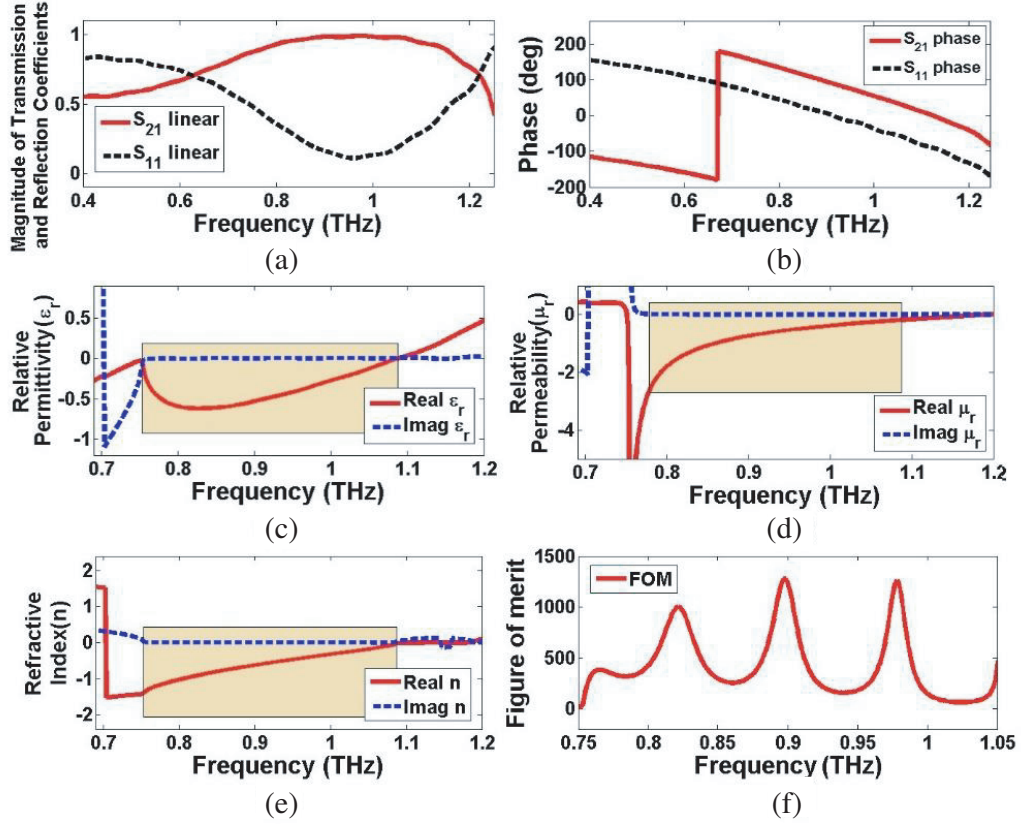
Figure 2. (a) Magnitude and (b) phase of transmission (S_{21}) and reflection (S_{11}) coefficients of 3-D NI MTM. Real and imaginary parts of (c) relative permittivity, (d) relative permeability, and (e) refractive index. The negative index region is shaded between 0.75 and 1.09 THz. (f) Figure of merit of the designed structure.

as follows: The retrieved permittivity and permeability values of the 3-D MTM are assigned to a homogeneous slab of unit-cell thickness, and transmission/reflection coefficients are recalculated under normal incidence. It is witnessed that the designed slab shows a homogenization error of 2% which is calculated using the formula $\Delta = \sqrt{(T_{\text{homo}} - T_{\text{MTM}})^2 + (R_{\text{homo}} - R_{\text{MTM}})^2}$ (where T_{homo} and R_{homo} and T_{MTM} and R_{MTM} are the transmission and reflection coefficients of the homogeneous slab and metamaterial, respectively), and hence the transmission/reflection coefficients of the MTM are in fair agreement with the ideal homogeneous slab as shown in Fig. 3(a). Also, it is interesting to note that the MTM shows uniform transmission characteristics for various multi-layer thickness slabs as shown in Fig. 3(b). This feature verifies that the NI flat slab is effectively homogeneous.

In this structure, metallic cylindrical loops exhibit magnetic resonances while the cross components exhibit electric resonances. When EM waves are incident on one surface, their electric field components interact with the metal components, and due to the collective oscillation of electrons, a negative permittivity [33] region occurs. Also, the magnetic field components of the incident field induce electric currents inside the cylindrical loops which results in a negative permeability [34] region. If the MTM consists of simultaneous electric and magnetic resonances in the same frequency regime, such MTM exhibits a negative index of refraction. Since the structure is symmetric in all three principal directions, this structure is expected to exhibit left-handed behavior in all incident directions under normal incidence.

The surface currents presented for TE and TM planewave excitations at 0.95 THz in Figs. 4(a) and 4(b), respectively, show the presence of electric and magnetic resonances in the proposed structure. The black arrows represent the direction of the electric dipole moment in the MTM. The prominent arrows on the left/right (top/bottom) sides in Fig. 4(a) (Fig. 4(b)) indicates the anti-parallel oscillations
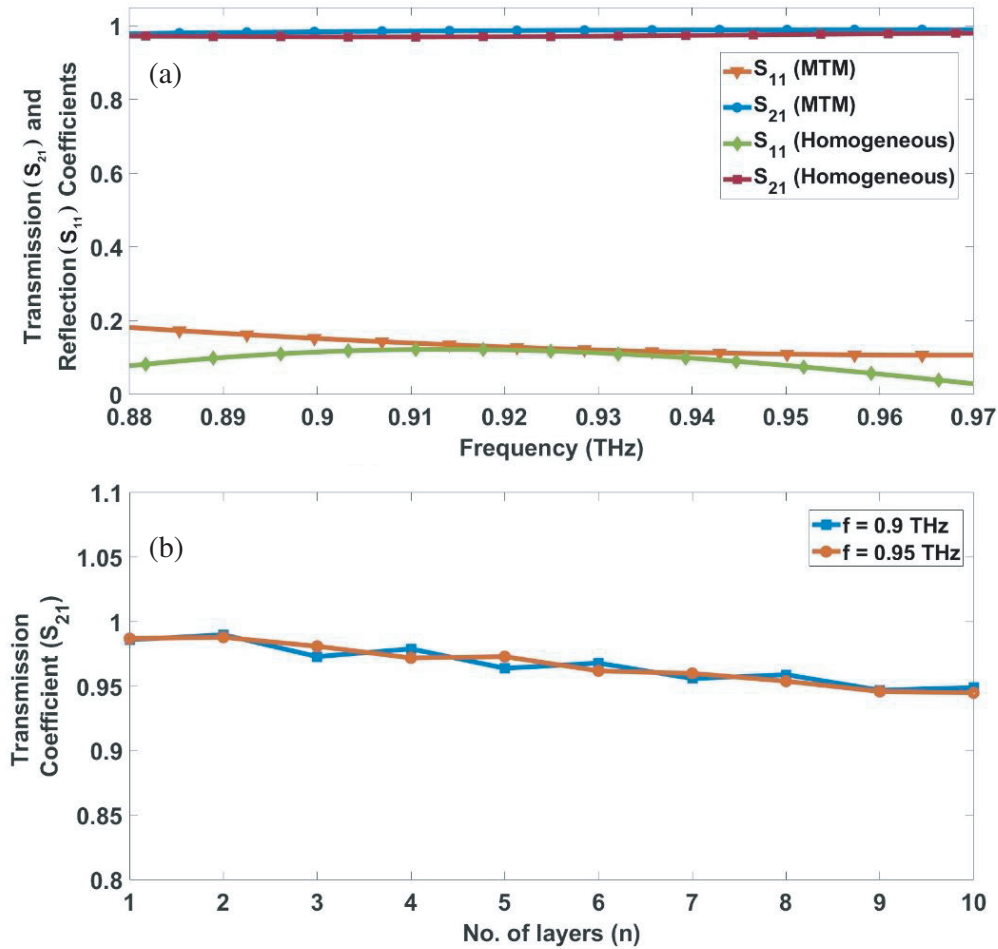
Figure 3. (a) Comparison of transmission and reflection coefficients of MTM and an ideal homogeneous slab whose constitutive parameters are equivalent to that of the MTM. (b) Transmission coefficients corresponding to 0.9 THz and 0.95 THz for different layers of unit cells stacked along z axis.

of electric dipoles for TE (TM) excitation. Since the anti-parallel oscillations of electric dipoles constitute a magnetic dipole, one would expect strong magnetic resonance in the proposed 3-D unit cell for both TE and TM excitations. Further, the magnetic response of the MTM for the incoming TE and TM planewaves can be visualized through the magnetic field maps shown in Figs. 4(c) and 4(d), respectively. As shown in Fig. 4(c) (Fig. 4(d)), when the magnetic field vectors of the incoming planewave oscillate along $\pm x$ ($\pm y$) directions for TE and TM waves, the magnetic field oscillations inside the MTM are along $\mp x$ ($\mp y$) directions, respectively, i.e., the induced current loops produce a magnetic field in a direction opposite to that of the incoming wave. This clearly shows the existence of magnetic resonance interaction in the proposed MTM.

2.3. 3-D NI MTM Behavior for Different Polarizations and Incident Angles

For analyzing the polarization and incident angle dependency of the proposed MTM, the unit cell structure is employed with input/output excitation ports along z directions with perfectly matched layers (PML) and with unit cell boundary conditions along x and y directions. To verify the polarization sensitiveness for the proposed 3-D NI MTM, the polarization angle (Ψ) of the incident TE plane wave is changed from $0°$ to $45°$, and the transmission coefficient is plotted in Fig. 4(e). It is observed that within the NI band, the transmission characteristics of the 3-D NI MTM unit cell are insensitive to the change of polarization angle.
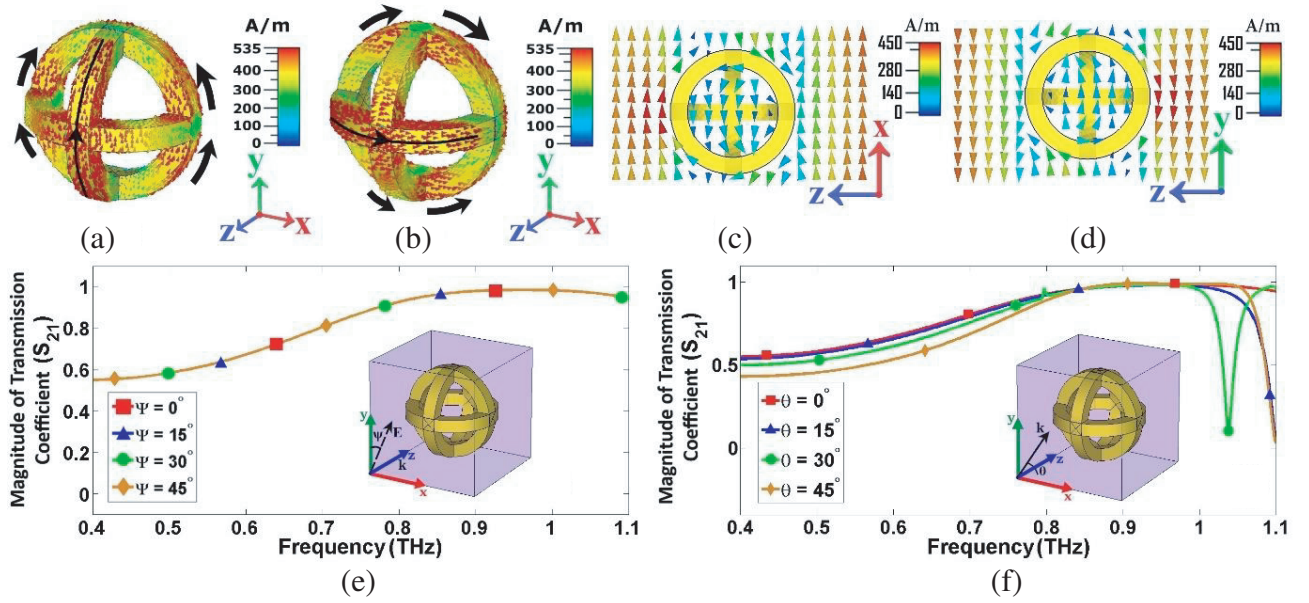
Figure 4. Surface current distributions in y-oriented NI MTM pattern at 0.95 THz for (a) TE and (b) TM plane wave excitations respectively. Magnetic field profile in the proposed NI MTM at 0.95 THz along (c) xoz plane for TE and along (d) yoz plane for TM excitations respectively. Transmission (S_{21}) characteristics: (e) for variation in polarization angle from 0° to 45° (Inset shows the schematic used for the polarization angle variation) and (f) for variation in incident angle from 0° to 45° (Inset shows the schematic used for the incident angle variation).

The non-normal incidence behavior of the 3-D NI MTM with the proposed unit cell is studied for the effects of exciting TE plane waves with oblique incidences elevated from the xoz-plane. Due to the symmetry of the proposed unit cell, it is sufficient to consider the incidence angle's (θ) variation between 0° to 45°. Fig. 4(f) shows the transmission coefficient of a 3-D unit cell for incident angle variation under TE plane wave excitation. It is ensured that the high transmission regime is quite insensitive to incident angle variations up to 30°.

Further, the responses of MTM for simultaneous variations of azimuthal and elevation angles of incidences are mapped as a surface transmission plot for TE plane wave excitations as shown in Fig. 5. It is observed that the corner contours of the surface plot reveal different transmission levels and thus the existence of anisotropy in the proposed 3-D MTM at the higher azimuthal and elevation angles. The reason for the existence of anisotropy is further examined through the visualization of different coupling between induced electric/magnetic dipole moments with the external EM waves in the proposed MTM using surface current analysis.

From Fig. 6, it is noted that when the incident angle of the incoming TE plane wave is varied as 15°, 30°, and 45°, not only the strength of the surface current in 3-D MTM decreases but also its distribution changes. For instance, surface current distribution at 45° is asymmetric so that different interaction coupling ($U_{\text{interaction}} = -\vec{p}_{\text{induced}} \cdot \vec{E}_{\text{incident}}$) is expected between the induced electric dipole moment ($\vec{p}_{\text{induced}}$) of the MTM and the external electric field of the incident wave ($\vec{E}_{\text{incident}}$). A similar interaction is also expected for magnetic dipole moments and the magnetic field strength of the incident wave. As the surface-area interaction of the incoming waves decreases for increasing incident angles, the coupling between the air-MTM interface decreases. Thus, the reduction in the effective area of the MTM for higher angles of incidence is attributed to why the proposed 3-D MTM exhibits different responses at higher angles of incidence despite the four-fold symmetry of the proposed design.
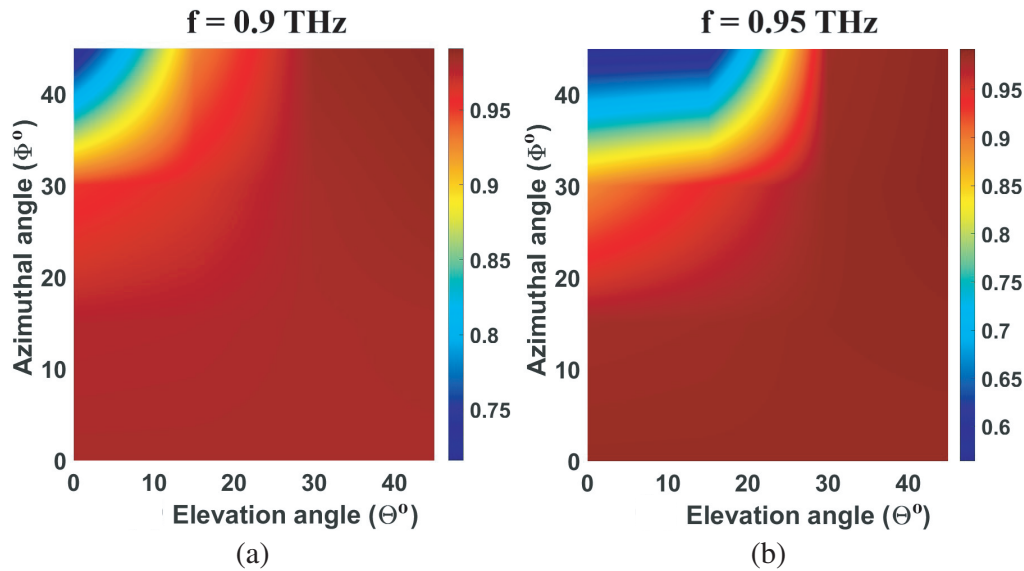
Figure 5. Surface plots of transmission coefficients of the proposed 3-D MTM for different elevation and azimuthal angles corresponding to (a) 0.9 THz and (b) 0.95 THz for TE polarization.
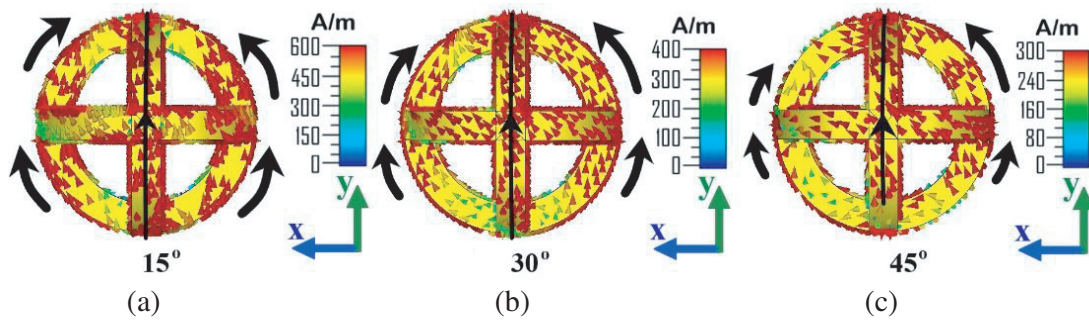

Figure 6. Surface current distributions in a unit cell in y-oriented NI MTM pattern at 0.95 THz for TE plane wave excitations with angles of incidence (a) 15°, (b) 30° and (c) 45° respectively.

3. DESIGN OF FLAT LENS AND ITS APPLICATIONS

3.1. Flat Lens Construction

A standard convex lens uses refraction properties to focus the incoming light. However, a standard flat plate made of positive index will not focus anything. It is known that with the help of NI MTMs [35], focusing with the flat profile is achievable for an omnidirectional source. Though the theory of flat lens imaging is well established [36], for construction purposes, the focusing ray diagram by the NI flat lens is given in Fig. 7(a). Cylindrical waves emerging from a line source (current carrying thin cylindrical conducting wire can be used as a cylindrical wavefront source of TE polarization) located near such an NI lens will first be refracted through the first air-NI slab interface and will bend into a focus inside the slab. After the first focusing, emergent waves will undergo refraction again at the second NI slab-air interface, and the refracted beam will bend towards the optical axis of the flat lens, where the second focusing will occur as described in Fig. 7(a). The flat slab should be thick enough for the first focusing to occur inside the lens, which results in a converging beam. Otherwise, a thin slab leads to a diverging beam which will not show the double focus anywhere. Hence, the choice of thickness of the lens or number of layers of NI slab plays a vital role in observing a flat lens behavior.
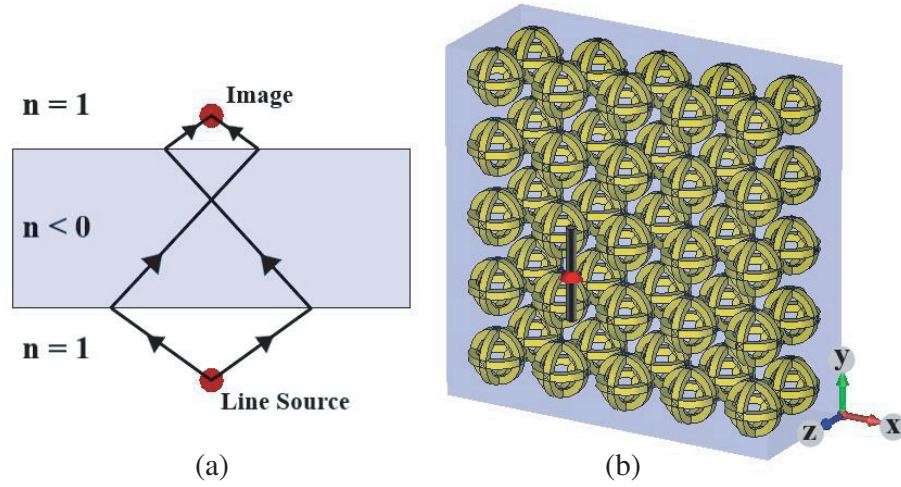
Figure 7. (a) Scheme of double refraction in an NI slab. (b) Electric dipole antenna placed in front of 3-D NI MTM slab.

In this work, we designed an NI flat slab with five-unit cells along each transversal direction and two such layers along the propagation direction as shown in Fig. 7(b). The numerical analysis of the flat lens is made with the transient calculations where the finite geometry is employed with open boundaries along all directions. The geometry is excited with a dipole antenna corresponding to two different frequencies in the NI region as shown in schematic Fig. 7(b). The electric dipole antenna is designed with each arm length $L \simeq 92\,\mu\text{m}$, diameter $D = 6\,\mu\text{m}$, and separation gap $g \simeq 0.92\,\mu\text{m}$, and fed with a feed line of $I = 1\,\text{A}$ alternating current between the two arms.

3.2. Flat Lens for Sub-Wavelength Focusing

When the dipole antenna excited with frequency f_1 (0.9 THz), is placed at a distance of $90\,\mu\text{m}$ ($0.27\lambda_1$), the focal spot is observed at $342\,\mu\text{m}$ ($1.03\lambda_1$) measured from the front surface of the slab. Figs. 8(a) and 8(b) show the electric field distributions ($|\text{Re}(E_{\text{abs}})|$) at 0.9 THz on both sides of the NI slab along the *yoz*- and *xoz*-planes, respectively. It is evident that the flat NI slab shows focusing functionality for the incoming diverging beam emitted from a dipole-line source. The bright spots concentrated at the back side of the NI flat slab show that it behaves as a converging lens for the incoming cylindrical waves. Moreover, the electric field distributions ($|\text{Re}(E_{\text{abs}})|$) shown for the *yoz*-plane (Fig. 8(a)) and *xoz*-plane (Fig. 8(b)) reveal clear focusing formed on the other side. To depict the size of the focusing spot, magnitudes of electric field intensity profile ($|E_{\text{abs}}|^2$) are scanned along the transverse direction and plotted as shown in Fig. 8(c). The spot size predicted from the full-width at half-maximum (FWHM) of the intensity profile is $0.48\lambda_1$ along the transversal direction (*x*-axis).

Also, the focusing efficiency of the proposed NI flat lens is calculated to be around 56%. The focusing efficiency is calculated as the ratio of the optical intensity in the focal plane to that of the incident plane. The incident beam intensity is defined as the optical intensity passing through an aperture with the same dimensions as that of the NI flat lens.

The numerical aperture (NA) of the proposed NI flat lens is found to be 0.94 which is quite high and causes focusing near the lens. It is calculated by using the expression $\text{NA} = n_{\text{back}} \sin \varphi$, where n_{back} is the effective refractive index of the environment in which the lens is placed. The acceptance angle φ is given by $\varphi = \tan^{-1}(H/2F)$ where H is the height of the lens, and F is its focal length.

Similarly, to assert the wideband NI of 3-D MTM and deep sub-wavelength focusing, the image formation due to the dipole-line source for the same source distance $90\,\mu\text{m}$ ($0.28\lambda_2$) is numerically analyzed for another frequency f_2 (0.95 THz). Figs. 9(a) and 9(b) show the electric field distributions ($|\text{Re}(E_{\text{abs}})|$) at 0.95 THz on both sides of the NI slab along the *yoz*- and *xoz*-planes, respectively. The intensity profile ($|E_{\text{abs}}|^2$) traced along the transverse direction is plotted as shown in Fig. 9(c), and the measured spot size is $0.39\lambda_2$ along the *x*-axis centered at the focal spot which is observed at $362.7\,\mu\text{m}$
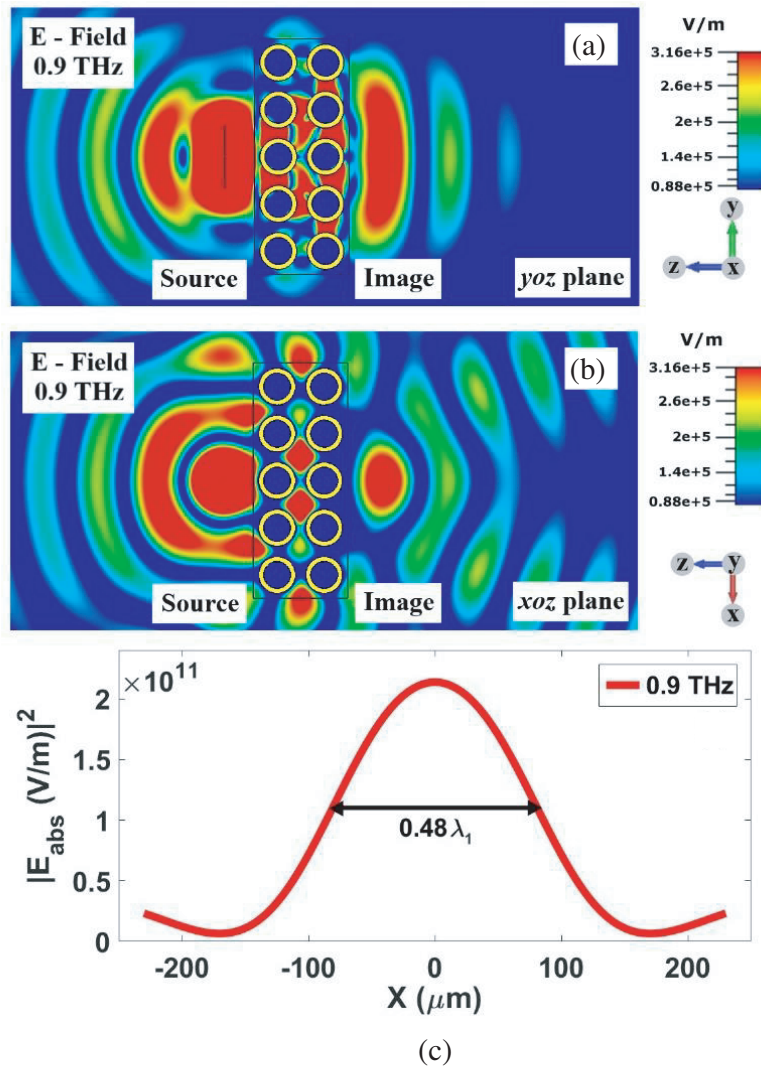
Figure 8. Absolute values of real part of electric field ($|\mathrm{Re}(E_{\mathrm{abs}})|$) distribution at 0.9 THz shows focusing by NI slab due to a dipole-line source along (a) yoz-plane and (b) xoz-plane. (c) Transverse scanning profile of absolute values of electric field intensity ($|E_{\mathrm{abs}}|^2$) at focused spot along x-axis and its measured FWHMs is $0.48\lambda_1$. Source distance and focal distance measured from the front face are $0.27\lambda_1$ and $1.03\lambda_1$ respectively.

$(1.15\lambda_2)$ from the front face of the NI slab.

The difference in focal distances for different frequencies is mainly due to the dispersive nature ($n(\omega)$) of the MTM, and it is evident from the effective material parameters shown in Fig. 2. The measured FWHM significantly represents the sub-wavelength focusing. It is comparatively smaller than what would be expected from a conventional positive index lens. Also, the focal point is falling in the extreme near-field region of the NI slab, and it has a resolution that is much smaller than the wavelength.

As the thickness of the NI flat slab plays a major role in double refraction, the functional band of the designed 2-layer NI lens is analyzed for the same source distance, 90 μm. Sub-wavelength focusing is observed for frequencies between 0.88 THz and 0.96 THz (24% of NI band) with the proposed NI flat slab, and the corresponding spot sizes are listed in Table 1. It is useful to note that to attain sub-wavelength focusing for other frequencies in NI band, the thickness (number of layers) of the NI slab and source distance need to be altered for appropriate dimensions.
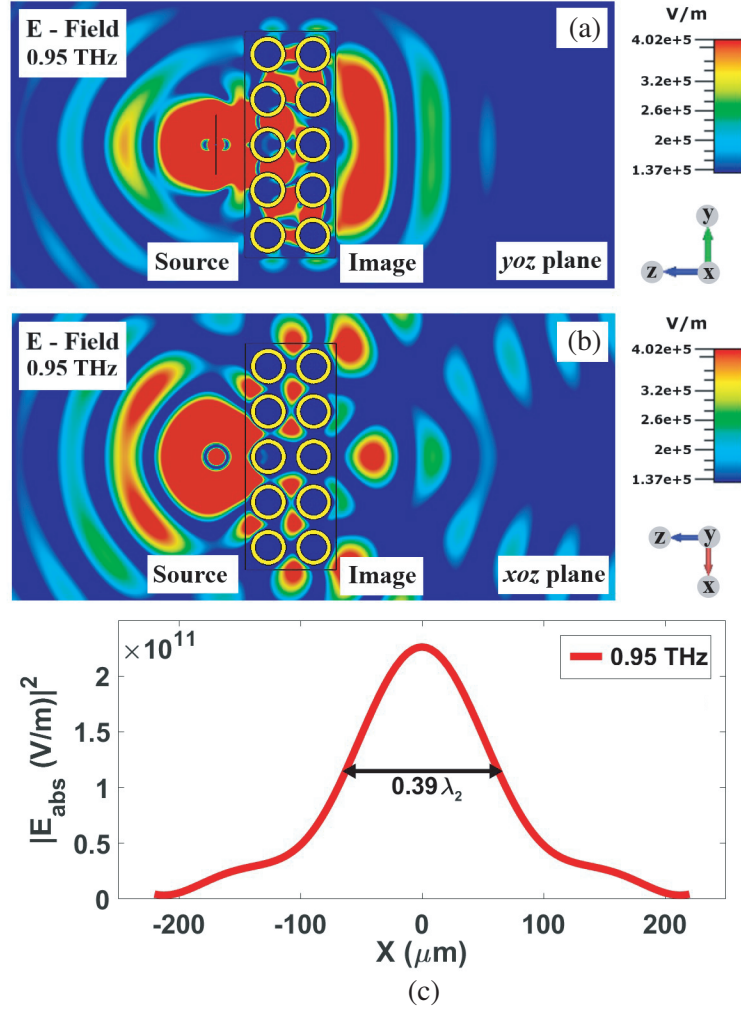
Figure 9. Absolute values of real part of electric field ($|\mathrm{Re}(E_{\mathrm{abs}})|$) distribution at 0.95 THz shows focusing by double negative (DNG) slab due to a dipole-line source along (a) *yoz*-plane and (b) *xoz*-plane. (c) Transverse scanning profile of absolute values of electric field intensity ($|E_{\mathrm{abs}}|^2$) at focused spot along *x*-axis and its measured FWHMs is $0.39\lambda_2$. Source distance and focal distance measured from the front face are $0.28\lambda_2$ and $1.15\lambda_2$ respectively.

Table 1. Calculated spot sizes for different frequencies.

m	f_m	**FWHM**
1	0.88 THz	$0.49\lambda_m$
2	0.90 THz	$0.48\lambda_m$
3	0.92 THz	$0.46\lambda_m$
4	0.94 THz	$0.42\lambda_m$
5	0.96 THz	$0.38\lambda_m$

The 3-D focusing feature of the NI flat slab can be revealed by analyzing the image formation by rotating a line source for various tilting angles. Supposing a flat lens produces uniform focal spot irrespective of the source's orientation, one can affirm the 3-D focusing signature of the proposed MTM. Hence, considering the four-fold symmetry of the NI flat slab, its focusing behavior is analyzed at
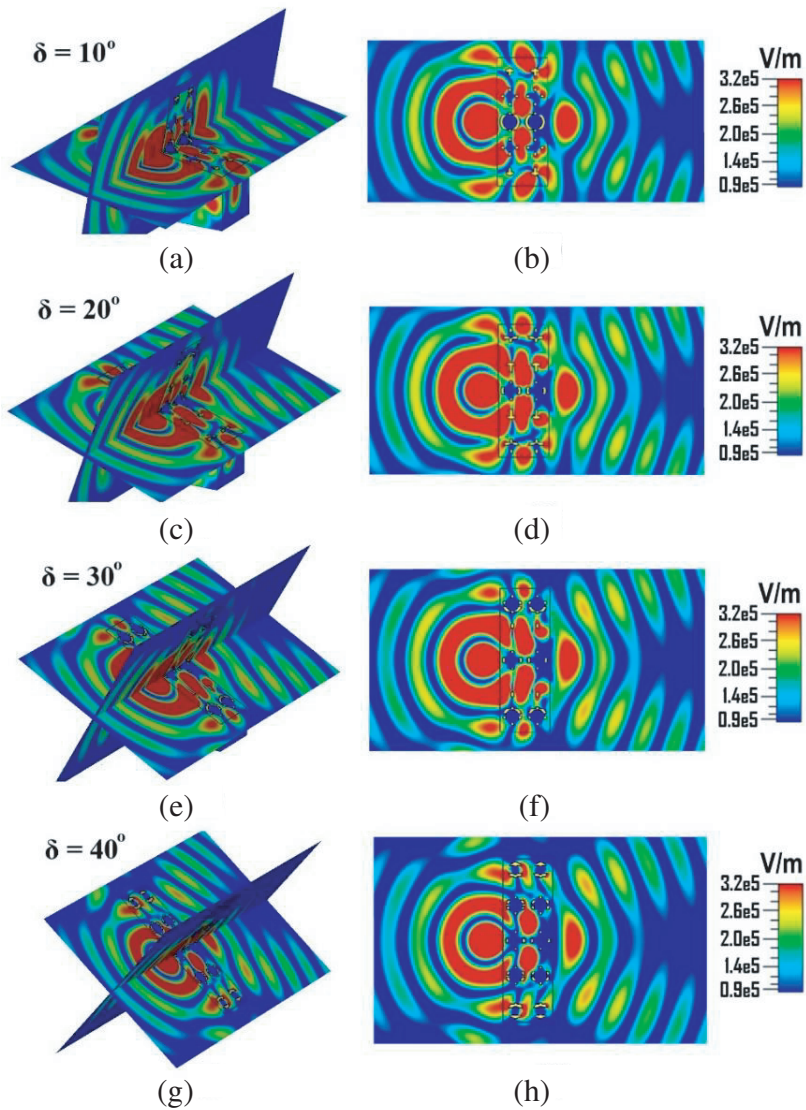
Figure 10. Absolute values of real part of electric field ($|\mathrm{Re}(E_{\mathrm{abs}})|$) distribution at 0.9 THz shows focusing by NI slab due to dipole-line source tilted along non-symmetric planes. 3-D view and azimuthal plane view corresponding to line source tilted angle (a)–(b) $\delta = 10°$, (c)–(d) $\delta = 20°$, (e)–(f) $\delta = 30°$ and (g)–(h) $\delta = 40°$ respectively.

0.9 THz for a line source tilting angles (δ) from $10°$ to $40°$ in steps of $10°$. For all the tilting cases, the flat slab exhibits focusing behavior along the corresponding focal planes as shown in Fig. 10. Also, the spot size of the focus formed is the same as in the case of the y-oriented line source. It is evident that the proposed NI flat slab with 3-D MTM can focus the incoming cylindrical waves, irrespective of the orientation of a line source, and this aspect reveals the 3-D focusing signature of the proposed NI flat slab.

3.3. Linearity and Reciprocity of Flat NI Slab

Double refraction in an NI medium mainly depends on the source distance, thickness, and the aperture size of the slab. For the given configuration, the source's distances are varied, and their corresponding focal distances are numerically calculated. It is noticed that for a wide range of source distances from the flat surface, clear images of the source are subsequently observed. When the source is moved towards
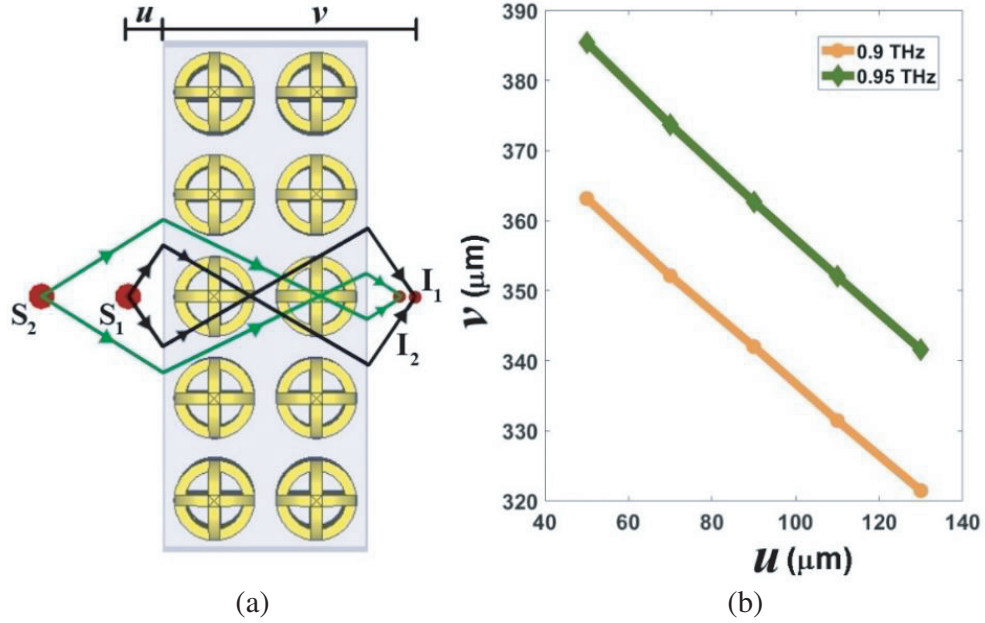
(a)   (b)

Figure 11. Variation of focusing distance with source's distance. (a) Schematic view of double refraction in NI MTM slab for various source distances. (b) The linear variation of focusing distance with respect to the source's distance corresponds to 0.9 THz and 0.95 THz respectively.

the flat surface, the focusing formed on the other side moves away from the slab. As shown in Fig. 11(a), when the source S_2 is placed at a farther distance from the slab, image I_2 is observed very close to the slab whereas image I_1 corresponding to the nearby source S_1 is observed at a larger distance. From Fig. 11(b), it is evident that the NI slab shows linearity between the source and focal distances for two different NI frequencies 0.9 THz and 0.95 THz. Also, the measured spot sizes, as shown in Table 2, are in sub-wavelength dimensions for a wide range of source distances. It is also observed that the NI flat slab's functionality remains the same when the source is kept at the depicted focal spot, which signifies its reciprocity functionality. Hence, for imaging devices using the proposed NI slab, the source transmitting end and receiving focal ends can be interchanged.

Table 2 shows the depicted spot sizes and focusing distances (v) corresponding to the dipole source at various distances (u) measured from the front face of the NI slab.

Table 2. Variation of focusing distance in the NI flat lens with respect to source distance.

Source Distance $u(\mu m)$	$f_1 = 0.9\,\text{THz}$		$f_2 = 0.95\,\text{THz}$	
	Focusing Distance v (μm)	Spot Size FWHM	Focusing Distance v (μm)	Spot Size FWHM
50	363.16 ($1.09\lambda_1$)	$0.50\lambda_1$	385.41 ($1.22\lambda_2$)	$0.38\lambda_2$
70	352.14 ($1.06\lambda_1$)	$0.49\lambda_1$	373.72 ($1.18\lambda_2$)	$0.39\lambda_2$
90	342.03 ($1.03\lambda_1$)	$0.48\lambda_1$	362.70 ($1.15\lambda_2$)	$0.39\lambda_2$
110	331.47 ($0.99\lambda_1$)	$0.48\lambda_1$	352.03 ($1.11\lambda_2$)	$0.40\lambda_2$
130	321.47 ($0.96\lambda_1$)	$0.46\lambda_1$	341.58 ($1.08\lambda_2$)	$0.41\lambda_2$

3.4. NI Slab Acting as an Effective THz Beam Translator

It is noted that the proposed NI MTM medium shows high transmission left-handed behavior in its NI regime, and hence it is expected that the radiated field components entering the front face will be transmitted to the other end. To analyze the propagation of THz beams for longer conveyance lengths, the NI slabs are stacked into different layers and excited with a Gaussian beam [37]. A Gaussian beam is a radially diverging beam where its electric field distribution along the perpendicular planes is provided by a parabolic phase profile.

Since a Gaussian beam acquires a positive phase (diverging) curvature while propagating in a positive refractive index medium, the peak intensity of the subsequent crests decreases in magnitude. When the Gaussian beam is introduced into a negative refractive index medium [37], it acquires a negative phase (converging) curvature, under paraxial approximation as shown in Fig. 12.
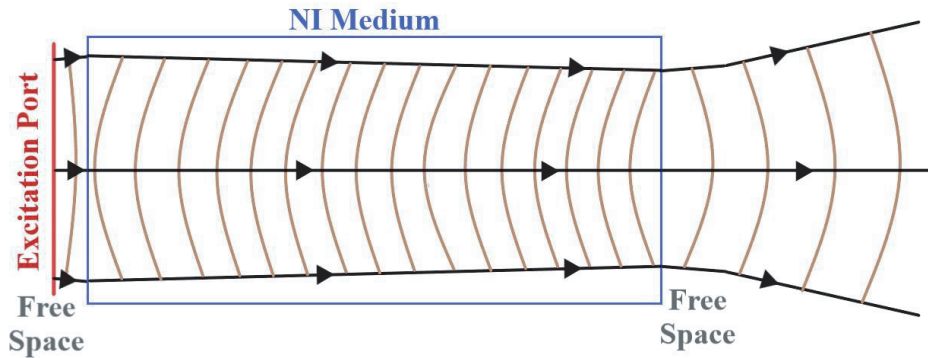

Figure 12. Illustration of Gaussian beam translation in NI medium.

Thus, an NI medium is capable of focusing the incoming diverging waves inside it which leads to beam translation behavior. It is interesting to note from Fig. 11(a) that after the first focus inside the NI medium, the THz rays travel without any deviation until it reaches the second interface. If the length of the DNG medium is increased along the propagation direction, the radiated field components will travel further with minimal loss. Due to the negative refraction at the second interface between air $(n = +1)$ and NI medium $(n = -1)$, the diverging waves are refocused, and it recovers the waist of the intensity of the beam.

To analyze the propagation of EM waves in NI MTM medium, the flat slabs are stacked into multiple layers, and they are excited with diverging Gaussian beams. Electric field distributions $(|\text{Re}(E_{\text{abs}})|)$ and longitudinal scanning profiles $(|E_{\text{abs}}|^2)$ in Fig. 13 show the comparison of propagation of the Gaussian beam in free space with multiple layers of NI MTM slabs at 0.816 THz. When THz Gaussian beams are traveling in free space for a conveyance length of 4λ, around 6.97 dB (79.9%) peak intensity loss is observed whereas in 10-layer NI MTM medium ($\sim 4\lambda$), around 0.24 dB (5.4%) peak intensity loss is observed. Since the majority of the incoming waves are guided within the NI MTM slabs, limited to the incident angles, efficient beam transfer is observed. Figs. 13(c)–(d), (e)–(f), and (g)–(h) show the electric field distributions and intensities along the z-axis, corresponding to 10-layers, 15-layers, and 20-layers NI MTM slabs, respectively. It can be noted that, in the case of NI medium, most of the electric field components are directed along the propagation direction, i.e., the z-axis.

Similarly, when Gaussian beams are transmitted through NI medium with longer conveyance lengths, the peak intensity losses of 0.34 dB (7.44%) and 0.39 dB (8.65%) are observed, corresponding to 15-layer ($\sim 6\lambda$) and 20-layer ($\sim 8\lambda$) NI MTM slabs, respectively. Beam divergence is the angular measure of the increasing radius of the beam with respect to the increasing distance. The divergence angle is given by the relation $\Theta = \Delta FWHM/\Delta Z$, where $\Delta FWHM$ is the difference in beam widths measured along two planes perpendicular to the propagation direction, and ΔZ is the distance between them. To analyse the beam divergence due to the proposed NI slabs, beam profiles along the incoming and emergent z-planes are considered as shown in Fig. 13(c). For the case of 10-layers, 15-layers, and 20-layers NI slabs, the divergence angles of $-1.12°$, $-0.53°$, and $+0.02°$ are observed, respectively. On
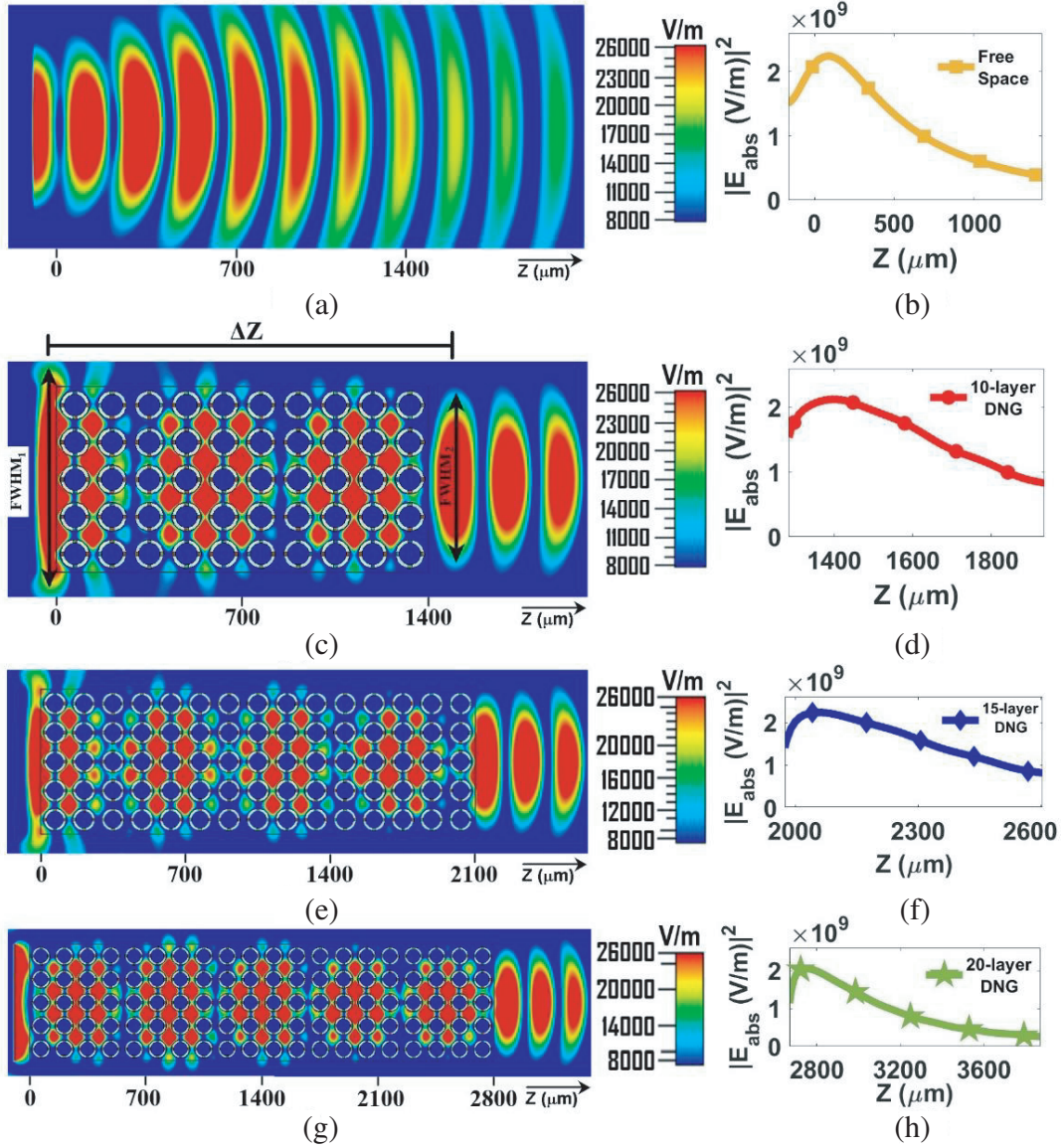
Figure 13. Electromagnetic beam translation in NI MTM medium. Absolute values of real part of electric field ($|\mathrm{Re}(E_{\mathrm{abs}})|$) distribution along yoz-plane and longitudinal scanning of absolute values of electric field intensity ($|E_{\mathrm{abs}}|^2$) profiles along a propagation direction corresponding to (a)–(b) free space, (c)–(d) 10 layers, (e)–(f) 15 layers and (g)–(h) 20 layers NI MTM slabs respectively.

the other hand, when the Gaussian beams are traveling in free space, the divergence angle of $+28.94°$ is observed for a distance of nearly 4λ. The negative and low divergence angle signifies the convergence due to NI slabs and its efficient beam transfer characteristics.

Hence, one can expect that the NI medium translates the Gaussian beam profile as well as the intensity of incoming THz waves from one location to another with a low loss feature. Due to the low transmission loss, the proposed NI medium is capable of controlling light propagation for longer distances. It is useful to note that the beam transferring property of NI media may lead to the design of optical devices that requires controlled wave propagation and beam translation [38, 39].

Hence, from this study, the following strands are observed: The proposed unit-cell is 3-D symmetric with a wide NI regime at THz frequencies, and it shows that the behavior of the proposed unit cell is independent of the incident direction (x or y or z), and hence the functionality is the same in all three

principal directions. From the transmission properties, it is also noted that the functionality of the unit cell is independent of the polarization angle. The surface transmission plots shows that the unit cell's functionality remains the same for simultaneous variations in incident azimuthal and elevation angles. Also, the left-handed behavior of the MTM is observed for a wide range (up to 30°) of non-normal incident angles which is evident from the surface current analysis. The flat NI slab designed with the proposed NI MTM focuses the incoming cylindrical waves from an electric dipole source in the near-field region with sub-wavelength resolution. Its focusing characteristics remain uniform along both symmetric and non-symmetric planes. It is essential to note that the resolution of the designed lens is higher for a wide range of source distances and for different frequencies in NI band. Also, due to the 3-D functionality of the NI MTM, the proposed flat lenses showed linearity and reciprocity between source and focusing positions. The field restoration by the NI medium is evident from the peak intensities observed on their emerging sides. The low-loss transmission of THz beams for longer propagation lengths is analyzed for different layer stackings of NI MTM slabs, and it is compared with free space. These results establish that the proposed 3-D NI MTM serves as an efficient electromagnetic beam translator with minimal losses for the incoming THz waves.

The fabrication of such proposed MTM-based THz optical elements can be done with widely used technologies such as multiphoton microfabrication [40], super-fine-ink-jet (SIJ) printing [41], direct laser writing (DLW) [42], mask-directed micro-3D printing [43], and focused ion beam — stress-induced deformation (FIB-SID) method [44]. Multiphoton microfabrication technique is used to fabricate 3-D microstructures with a submicron resolution by DLW with a femtosecond pulsed laser beam. Alternatively, FIB-SID is an ideal tool to construct various 3-D optical micro and nanostructures with flexible and complex geometries which utilize induced surface stress to bend the cantilever upward or downward. Especially, we notice that in [44], hybrid fabrication with the combination of 3-D printing, metal coating, and wet etching has been proposed to fabricate the 3-D ring MTM geometries with high accuracy. Nowadays, micro 3D printing (μ-3DP) based on mask-directed multiphoton lithography (MDML) is used for fabricating complex 3D prototypes assisted by computer-aided design (CAD). In this approach, unique and predictable features could be generated using masks that act as projection tools for the fabrication of geometries in traditional photolithography. Some of the recent experimental works [45–49] show that structurally complex, 3-D microstructures can be fabricated. These techniques have the greatest potential to manufacture 3-D microscale and structurally complex MTM as it provides intrinsic sub-micron resolution for 3-D structures. Therefore, we anticipate that the proposed 3-D MTM geometry can be fabricated successfully.

4. CONCLUSION

To conclude, a 3-D negative refractive index MTM is proposed which has a negative refractive bandwidth of 0.34 THz (relative bandwidth 37%) centered at 0.92 THz. An NI flat slab is designed out of the proposed 3D NI MTM unit cells which behaves as a converging lens for the incoming diverging beams from an omnidirectional source along both symmetric and non-symmetric planes. The depicted transversal electric field intensity distribution showed bright sub-wavelength-sized focusing spots for various source positions corresponding to different frequencies in the NI band. Also, the potential of the NI slab as an electromagnetic beam translator is demonstrated. These results confirm that sub-wavelength focusing by NI MTM is realizable at THz frequencies and the ability of the proposed MTM to beat the diffraction limit offers several applications of lenses, imaging, and beam transfer applications in THz waveband. The feasible fabrication aspects were highlighted to show the practical realization of the proposed 3-D MTM.

REFERENCES

1. Veselago, V. G., "The electrodynamics of substances with simultaneously negative values of ε and μ," *Sov. Phys. Usp.*, Vol. 10, 509, 1968.
2. Pendry, B., "Negative refraction makes a perfect lens," *Phys. Rev. Lett.*, Vol. 85, 3966, 2000.
3. Padilla, W. J., D. N. Basov, and D. R. Smith, "Negative refractive index metamaterials," *Materials Today*, Vol. 9, Nos. 7–8, 28–35, 2006.

4. Xu, T., A. Agrawal, M. Abashin, K. J. Chau, and H. J. Lezec, "All-angle negative refraction and active flat lensing of ultraviolet light," *Nature*, Vol. 497, 470–474, 2013.

5. Yang, Q., J. Gu, D. Wang, X. Zhang, Z. Tian, C. Ouyang, R. Singh, J. Han, and W. Zhang, "Efficient flat metasurface lens for terahertz imaging," *Opt. Express*, Vol. 22, 25931–25939, 2014.

6. Zhang, X. C., "Terahertz wave imaging: horizons and hurdles," *Phys. Med. Biol.*, Vol. 47, No. 21, 3667–3677, 2002.

7. Withayachumnankul, W. and D. Abbott, "Metamaterials in the terahertz regime," *IEEE Photonics Journal*, Vol. 1, No. 2, 99–118, 2009.

8. Asrafali, B., C. Venkateswaran, and N. Yogesh, "Spatially squeezed electromagnetic modes of a transformational optics based cavity resonator for targeted material heating," *Progress In Electromagnetics Research M*, Vol. 106, 205–214, 2021.

9. Zimdars, D., J. A. Valdmanis, J. S. White, G. Stuk, S. Williamson, W. P. Winfree, and E. I. Madaras, "Technology and applications of terahertz imaging non-destructive examination: Inspection of space shuttle sprayed on foam insulation," *AIP Conf. Proc.*, Vol. 760, 570–577, 2005.

10. Hu, B. B. and M. C. Nuss, "Imaging with terahertz waves," *Opt. Lett.*, Vol. 20, No. 16, 1716–1718, 1995.

11. Lei, Y., B. Liang, S. Zhuang, and G. Wang, "Subwavelength focusing by combining negative-refractive photonic crystal and silicon lens," *Opt. Mater. Express*, Vol. 9, 3962–3967, 2019.

12. Suzuki, T., M. Sekiya, T. Sato, and Y. Takebayashi, "Negative refractive index metamaterial with high transmission, low reflection, and low loss in the terahertz waveband," *Optics Express*, Vol. 26, No. 7, 8314–8324, 2018.

13. Bilal, R. M. H., M. A. Baqir, A. Iftikhar, M. M. Ali, A. A. Rahim, M. N. Akhtar, M. J. Mughal, and S. A. Naqvi, "A novel omega shaped microwave absorber with wideband negative refractive index for C-band applications," *Optik*, Vol. 242, 2021.

14. Askari, M., Z. Touhidi Nia, and M. V. Hosseini, "Modified fishnet structure with a wide negative refractive index band and a high figure of merit at microwave frequencies," *J. Opt. Soc. Am. B*, Vol. 39, 1282–1288, 2022.

15. Chang, C.-L., W.-C. Wang, H.-R. Lin, F. J. Hsieh, Y.-B. Pun, and C.-H. Chan, "Tunable terahertz fishnet metamaterial," *Appl. Phys. Lett.*, Vol. 102, 151903, 2013.

16. Islam, S. S., M. S. Khan, and M. R. I. Faruque, "Design and analysis of modified-split-H-shaped DNG metamaterial for microwave application," *Mater. Res. Express*, Vol. 6, 125808, 2019.

17. Yeh, T. T., T. Y. Huang, T. Tanaka, and T.-J. Yen, "Demonstration of a three-dimensional negative index medium operated at multiple-angle incidences by monolithic metallic hemispherical shells," *Sci. Rep.*, Vol. 7, 45549, 2017.

18. Ding, J., S. An, B. Zheng, and H. L. Zhang, "Multiwavelength metasurfaces based on single-layer dual-wavelength meta-atoms: Toward complete phase and amplitude modulations at two wavelengths," *Adv. Opt. Mater.*, Vol. 5, No. 10, 1700079, 2017.

19. Hakim, M. L., T. Alam, M. S. Soliman, N. M. Sahar, M. H. Baharuddin, S. H. A. Almalki, and M. T. Islam, "Polarization insensitive symmetrical structured Double Negative (DNG) metamaterial absorber for Ku-band sensing applications," *Sci. Rep.*, Vol. 10, No. 12(1), 479, 2022.

20. Wegrowski, A., W.-C. Wang, C. Tsui, and P. Garu, "Negative refractive index modified fishnet enhancement by wire shift," *Mater. Res. Express*, Vol. 9, 095801, 2022.

21. Marishwari, M., V. Subramanian, Z. Ouyang, and N. Yogesh, "3-D metamaterial based terahertz planoconcave lenses for linearly and circularly polarized waves," *Progress In Electromagnetics Research B*, Vol. 98, 21–37, 2023.

22. Xu, S., J.-B. Liu, H. Wang, C.-K. Su, and H.-B. Sun, "Three-dimensional metacrystals with a broadband isotropic diamagnetic response and an all-angle negative index of refraction," *Opt. Lett.*, Vol. 44, 927–930, 2019.

23. Cheng, Y. Z., Y. Nie, and R. Z. Gong, "Broadband 3D isotropic negative-index metamaterial based on fishnet structure," *Eur. Phys. J. B*, Vol. 85, 62, 2012.

24. Liu, Y., G. P. Wang, J. B. Pendry, and S. Zhang, "All-angle reflectionless negative refraction with ideal photonic Weyl metamaterials," *Light: Sci. Appl.*, Vol. 11, 276, 2022.

25. Yang, Y., Y. Bi, L. Peng, B. Yang, S. Ma, H.-C. Chan, Y. Xiang, and S. Zhang, "Veselago lensing with Weyl metamaterials," *Optica*, Vol. 8, 249–254, 2021.

26. Zaremanesh, M. and M. Noori, "All-angle polarization-insensitive negative refraction in high-dielectric photonic crystal," *Appl. Opt.*, Vol. 58, 5631–5636, 2019.

27. Zharov, A., V. Fierro, and A. Celzard, "All-dielectric bulk isotropic double-negative metamaterials," *J. Opt. Soc. Am. B*, Vol. 38, 159–166, 2021.

28. Engheta, N., "Ideas for potential applications of metamaterials with negative permittivity and permeability" *Advances in Electromagnetics of Complex Media and Metamaterials. NATO Science Series*, S. Zouhdi, A. Sihvola, and M. Arsalane (eds.), Vol. 89. Springer, Dordrecht, 2002.

29. Tamosiunaite, M., S. Tamosiunas, and M. Z. A. Valusis,, "Atmospheric attenuation of the terahertz wireless networks," *Broadband Communications Networks — Recent Advances and Lessons from Practice*, 2017.

30. Yogesh, N. and V. Subramanian, "Analysis of self-collimation based cavity resonator formed by photonic crystal," *Progress In Electromagnetics Research M*, Vol. 12, 115–130, 2010.

31. Zheng, Y., Q. Wang, M. Lin, and Z. Ouyang, "Enhancement of self-collimation effect in photonic crystal membranes using hyperbolic metamaterials," *Nanomaterials (Basel)*, Vol. 12, No. 3, 555, 2022.

32. Lee, D. H. and W. S. Park, "Extraction of effective permittivity and permeability of periodic metamaterial cells," *Microw. Opt. Technol. Lett.*, Vol. 51, 1824–1830, 2009.

33. Pendry, J. B., A. J. Holden, D. J. Robbins, and W. J. Stewart, "Extremely low frequency plasmons in Metallic Mesostructures," *J. Phys. Condens. Lett.*, Vol. 10, 4785–4809, 1998.

34. Pendry, J. B., A. J. Holden, D. J. Robbins, and W. J. Stewart, "Magnetism from conductors and enhanced nonlinear phenomena," *IEEE Trans. Microwave Theory Tech.*, Vol. 47, 2075–2084, 1999.

35. Aydin, K., I. Bulu, and E. Ozbay, "Focusing of electromagnetic waves by a left-handed metamaterial flat lens," *Opt. Express*, Vol. 13, 8753–8759, 2005.

36. Ramakrishna, S. A. and T. M. Grzegorczyk, *Physics and Applications of Negative Refractive Index Materials*, 1st Edition, CRC Press, 2008.

37. Banerjee, P. P. and G. Nehmetallah, "Linear and nonlinear propagation in negative index materials," *J. Opt. Soc. Am. B*, Vol. 23, 2348–2355, 2006.

38. Engheta, N. and R. W. Ziolkowski, *Metamaterials — Physics and Engineering Explorations*, IEEE Press, 2006.

39. Ziolkowski, R., "Pulsed and CW Gaussian beam interactions with double negative metamaterial slabs," *Opt. Express*, Vol. 11, No. 7, 662–681, Apr. 7, 2003.

40. Maruo, S. and J. Fourkas, "Recent progress in multiphoton microfabrication," *Laser & Photon. Rev.*, Vol. 2, 100–111, 2008.

41. Takano, K., T. Kawabata, C.-F. Hsieh, K. Akiyama, F. Miyamaru, Y. Abe, Y. Tokuda, R.-P. Pan, C.-L. Pan, and M. Hangyo, "Fabrication of terahertz planar metamaterials using a super-fine ink-jet printer," *Appl. Phys. Express*, Vol. 3, 016701, 2010.

42. Rill, M. S., C. Plet, M. Thiel, I. Staude, G. von Freymann, S. Linden, and M. Wegener, "Photonic metamaterials by direct laser writing and silver chemical vapour deposition," *Nature Materials*, Vol. 7, 543–546, 2008.

43. Hernandez, D. S. and J. B. Shear, "Mask-directed micro-3D printing," *Micro and Nano Technologies, Three-Dimensional Microfabrication Using Two-Photon Polymerization (Second Edition)*, William Andrew Publishing, 2020.

44. Mao, Y., Z. Chen, J. Zhu, Y. Pan, W. Wu, and J. Xu, "Stereo metamaterial with three dimensional meta-atoms fabricated by programmable stress induced deformation for optical modulation," *IEEE 30th International Conference on Micro Electro Mechanical Systems (MEMS)*, 285–288, 2017.

45. Wang, Q., B. Gao, M. Raglione, H. Wang, B. Li, F. Toor, M. A. Arnold, and H. Ding, "Design, fabrication, and modulation of THz bandpass metamaterials," *Laser & Photonics Reviews*, Vol. 13, 1900071, 2019.

46. Reinbold, J., T. Frenzel, A. Münchinger, and M. Wegener, "The rise of (chiral) 3D mechanical metamaterials," *Materials (Basel)*, Vol. 12, No. 21, 3527, 2019.

47. Münchinger, A., L.-Y. Hsu, F. Fürniß, E. Blasco, and M. Wegener, "3D optomechanical metamaterials," *Materials Today*, Vol. 59, 9–17, 2022.

48. Huang, T.-Y., C.-W. Tseng, T.-T. Yeh, T.-T. Yeh, C.-W. Luo, T. Akalin, and T.-J. Yen, "Experimental realization of ultrathin, double-sided metamaterial perfect absorber at terahertz gap through stochastic design process," *Sci. Rep.*, Vol. 5, 18605, 2015.

49. Okatani, T., Y. Sunada, K. Hane, and Y. Kanamori, "Terahertz 3D bulk metamaterials with randomly dispersed split-ring resonators," *Nanophotonics*, Vol. 11, No. 9, 2065–2074, 2022.